J Mater Sci: Mater Electron **(2025) 36:141**

Synthesis, characterization, crystallization kinetics of amorphous $Fe_{74.5}Zr_{8.5}B_{17}$ magnetic nanoparticles, and magnetoelectric properties of $Fe_{74.5}Zr_{8.5}B_{17}$/$BaTiO_3$ composite

Gamze Dik[1], Emine Busra Kaplan[1], Ahmet Ulu[1,*], Nevzat Bayri[2], Burhan Ates[1], and Selcuk Atalay[2,*]

[1] *Faculty of Arts and Sciences, Department of Chemistry, Biochemistry and Biomaterials Research Laboratory, Inonu University, Malatya, Türkiye*

[2] *Faculty of Arts and Sciences, Department of Physics, Inonu University, Battalgazi, Malatya, Türkiye*

Received: 15 October 2024
Accepted: 27 December 2024
Published online: 15 January 2025

© The Author(s), 2025

ABSTRACT

This work reports the facile synthesis of amorphous $Fe_{74.5}$ $Zr_{8.5}$ B_{17} magnetic nanoparticles (MNPs) through a simple $NaBH_4$-assisted chemical reduction method. The obtained MNPs were characterized in terms of amorphous/crystal structure, morphology, magnetic properties, composition, and crystallization kinetics. The saturation magnetization value was determined as 57.83 emu/g. The crystallization peak temperatures (T_p) and activation energy were determined to be 467.18 °C and 294 kJ/mol, respectively. Additionally, the FeZrB MNPs were combined with the $BaTiO_3$ NPs via ball milling at low speed, using a mass ratio of 30/70%, respectively and the magnetoelectric coefficient value for FeZrB/$BaTiO_3$ composite measured at a 1 kHz AC magnetic field is approximately 8.9 mV/Oe/cm. The study outcomes may provide a platform of nanotechnology for the preparation of MNPs with adjustable properties, which will be promising for practical applications.

1 Introduction

Magnetic nanoparticles (MNPs) are an extremely important field that is open to development in many different fields, especially in physics and chemistry. MNPs can be obtained as crystalline or amorphous by changing the synthesis methods or synthesis conditions. Not having a crystal lattice provides amorphous MNPs with flexibility in manipulation and ease of use in various applications. This flexibility in manipulation enables the use of amorphous MNPs in the medical field, diagnosis, and treatment applications [1–5].

MNPs represent a fascinating and rapidly developing field at the intersection of physics, chemistry, and materials science. These small particles, typically ranging in size from 1 to several hundred nanometers, exhibit unique magnetic properties that distinguish them from their larger counterparts [6]. Their intriguing properties have spurred widespread interest and research due to their potential applications in fields

Address correspondence to E-mail: ahmet.ulu@inonu.edu.tr; selcuk.atalay@inonu.edu.tr

https://doi.org/10.1007/s10854-024-14186-9

ranging from medicine to electronics. Central to the importance of MNPs is their ability to respond to external magnetic fields, enabling precise manipulation and control [7]. This distinctive feature has paved the way for groundbreaking developments in the fields of targeted drug delivery, medical imaging, and magnetic hyperthermia, where MNPs generate heat for therapeutic purposes [8]. In particular, amorphous Fe ± Zr ± B alloy NPs are highly suitable for biomedical applications due to their diverse structural and magnetic properties, including their inhomogeneous spin structures and broad hyperin domain distributions, as well as their high-temperature resistivities [9]. However, there are also studies where FeZrB NPs or other NPs with magnetic properties are used as a composite with a structure such as $BaTiO_3$ in biomedical applications. There are two important advantages of using a magnetic material and $BaTiO_3$ together. The first one is that both materials are stable in more than one molecular phase without losing their characteristic properties. The other is extremely important in terms of ferroelectric and ferromagnetic effects in both materials [10, 11]. $BaTiO_3$, which exhibits ferroelectric properties, is a perovskite material with high permeability. $BaTiO_3$ can show successive phase transitions from orthorhombic to rhombohedral, tetragonal to orthorhombic, and cubic to tetragonal at different temperatures. In summary, unlike regular crystalline MNPs, amorphous FeZrB NPs do not have a well-defined and repeating structure [12]. Due to their amorphous properties, they offer a level of disorder that provides flexibility in various applications. This flexibility opens avenues for tailoring amorphous MNPs to meet specific needs, whether in materials science, medicine, or electronics. Preparation of these amorphous structures as composites with perovskite materials such as $BaTiO_3$ imparts various properties to the structure, such as ferroelectricity, pyroelectricity, and piezoelectricity [13]. In materials science, amorphous structures offer new possibilities for designing advanced materials with tailored properties.

The chemical reduction method is the most commonly used method for synthesizing amorphous MNPs. For example, according to the study reported by Forster et al. [9], they successfully prepared amorphous Fe–Zr–B MNPs by sodium borohydride reduction method. Here, they comprehensively investigated the reaction conditions and determined the optimum synthesis conditions. The Fe:Zr:B content ratios of the MNPs were also adjusted and it was determined that the MNPs with high iron content contained α-Fe crystals. On the other hand, Ramakrishna et al. [14] used the liquid chemical reduction method in the synthesis of Fe–Zr–B amorphous MNPs. They characterized the structure, morphology, and magnetic properties of the MNPs they synthesized through various analyses. Analysis showed that the nanoparticle size was below 30 nm and had an amorphous structure. In addition, the saturation magnetization value was determined as 55 emu/g [14].

In this study, the synthesis of amorphous Fe–Zr–B MNPs was achieved using the chemical reduction method. We also believe that it is very important to obtain information about amorphous MNPs and we consider the activation energy in amorphous MNPs as one of the key parameters in this context. Because, in material science, the process of crystallization unfolds as a transformative journey from disorder to order, giving rise to structures with defined symmetry and properties. At the heart of this intricate journey lies the concept of activation energy, a critical factor that intricately influences the kinetics and outcomes of crystallization processes. Understanding the importance of activation energy in crystallization not only unveils the mechanisms governing the formation of crystalline structures but also holds the key to optimizing and controlling the synthesis of materials with tailored properties. Only a few studies have been reported to date on the crystallization kinetics of amorphous MNPs [15–17]. To address the existing gap in the literature concerning the calculation of activation energy for amorphous MNPs, this study offers a comprehensive exploration of the synthesis, magnetic properties, and activation energy values of amorphous $Fe_{74.5}Zr_{8.5}B_{17}$ MNPs. For this purpose, the amorphous $Fe_{74.5}Zr_{8.5}B_{17}$ MNPs were successfully obtained by a simple chemical reduction method using $NaBH_4$ as a reduction agent (Fig. 1). Subsequently, the FeZrB MNPs were combined with the $BaTiO_3$ NPs via ball milling at low speed, using a mass ratio of 30/70%, respectively. The amorphous/crystal structure, surface morphology, magnetic properties, and elemental composition of the materials were characterized by several methods. Furthermore, to our best knowledge, the magnetoelectric properties of FeZrB/$BaTiO_3$ composites were investigated for the first time in the literature.

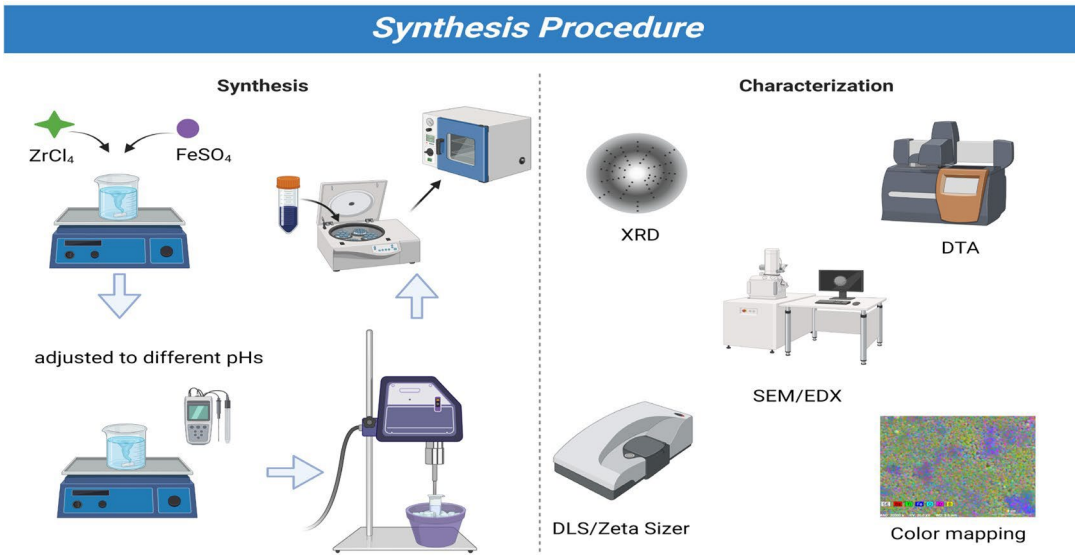

Fig. 1 Schematization of the experimental procedure. This figure was created with BioRender.com

2 Experimental

2.1 Materials

All chemicals were of analytical purity. $FeSO_4.7H_2O$ used in the synthesis of Fe–Zr–B amorphous MNPs was obtained from Carlo Erba (Milan, Italy). $ZrCl_4$ and NaOH were purchased from Sigma-Aldrich (St. Louis, MO). $NaBH_4$ was purchased from ABCR company. During the synthesis, the pH values of the solutions were determined using a pH meter (HIN2211 pH/ORP) belonging to HANNA instruments. During the synthesis of the MNPs, a Bandelin Sonopuls HD 2070 ultrasonic homogenizer (Bandelin Electronic GmbH & Co. KG, Berlin, Germany) was used to ensure the dispersion of the particles. All solutions used during the synthesis were prepared using pure water.

2.2 Synthesis of amorphous $Fe_{74.5}Zr_{8.5}B_{17}$ MNPs

Synthesis of amorphous $Fe_{74.5}Zr_{8.5}B_{17}$ MNPs was carried out according to the method stated in the literature [9]. Briefly, 10 g of $FeSO_4.7H_2O$ powder was dissolved in 100 mL of pure water. After the dissolution process was completed, 1.13 g of $ZrCl_4$ was added to this solution. After stirring for a while, the pH of the solution was adjusted using 0.1 M NaOH. While adjusting the pH, it was prepared by weighing 2.28 g of $NaBH_4$ to be added to the solution and dissolving it in 100 mL of pure water. The Fe-Zr solution, whose pH adjustment was completed, was placed in an ice-water bath and $NaBH_4$ solution was added dropwise onto the Fe-Zr solution in the presence of an ultrasonicator and dispersed for 30 min. After the completion of the period, the obtained MNPs were precipitated using a centrifuge and washed 3 times with pure water and 2 times with ethanol. Finally, the obtained MNPs were dried at 120 °C for 1.5 h. The steps of the synthesis are schematized in Fig. 2. There is a point that should be taken into consideration when examining this synthesis scheme. Before adding $NaBH_4$ in the synthesis process, the solution pH was adjusted to different values. We have calculated the percentage based on the ratios of the elements used during sample preparation.

2.3 Characterization

X-ray diffraction (XRD) characterization was used to estimate the amorphous or crystallinity nature of the materials. XRD spectra were recorded in the 2θ range 10–80° via powder X-ray diffractometer (Rigaku RadB-DMAX II). The surface morphology of synthesized MNPs was determined using scanning electron microscope (SEM, LEO Evo-40 VPX) and FESEM (Zeiss, Model: Gemini 500). The energy dispersive X-ray spectroscopy (EDX) analysis was performed by Röntec XFlash detector (model 125 eV; Bruker AXS, Berlin, Germany). The magnetization values of the samples were measured using a vibrating sample

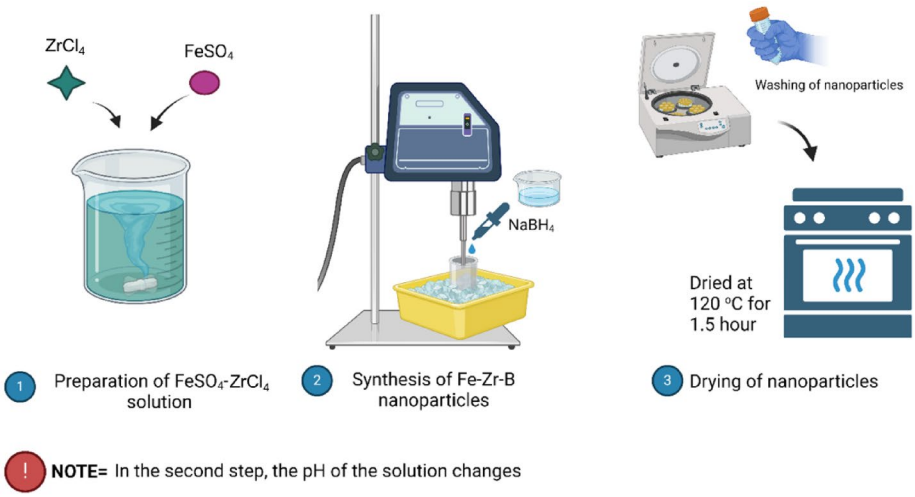

Fig. 2 Synthesis scheme of amorphous $Fe_{74.5}Zr_{8.5}B_{17}$ MNPs. This figure was created with BioRender.com

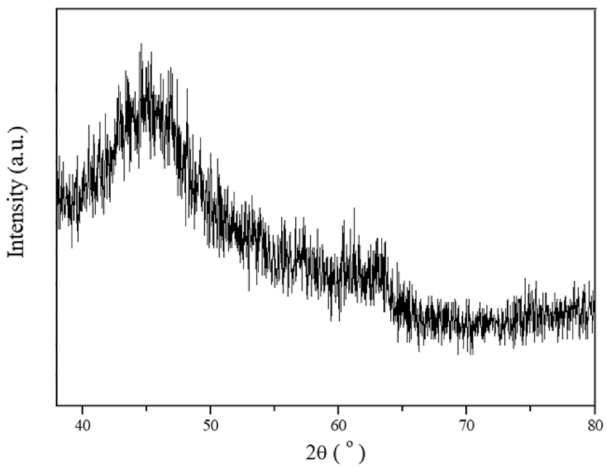

Fig. 3 The XRD patterns of $Fe_{74.5}Zr_{8.5}B_{17}$ MNPs

magnetometer (VSM) of a physical property measurement system (PPMS). The crystallization behaviors of the amorphous $Fe_{74.5}Zr_{8.5}B_{17}$ MNPs were studied using a Diamond PerkinElmer Differential Thermal Analysis (DTA) system.

3 Results and discussion

3.1 Amorphous FeZrB MNPs

The XRD data for amorphous $Fe_{74.5}Zr_{8.5}B_{17}$ MNPs are shown in Fig. 3. As can be seen here, very broad diffraction peaks characteristic of amorphous $Fe_{74.5}Zr_{8.5}B_{17}$ MNPs are observed for sample produced at pH 8 in Fig. 3.

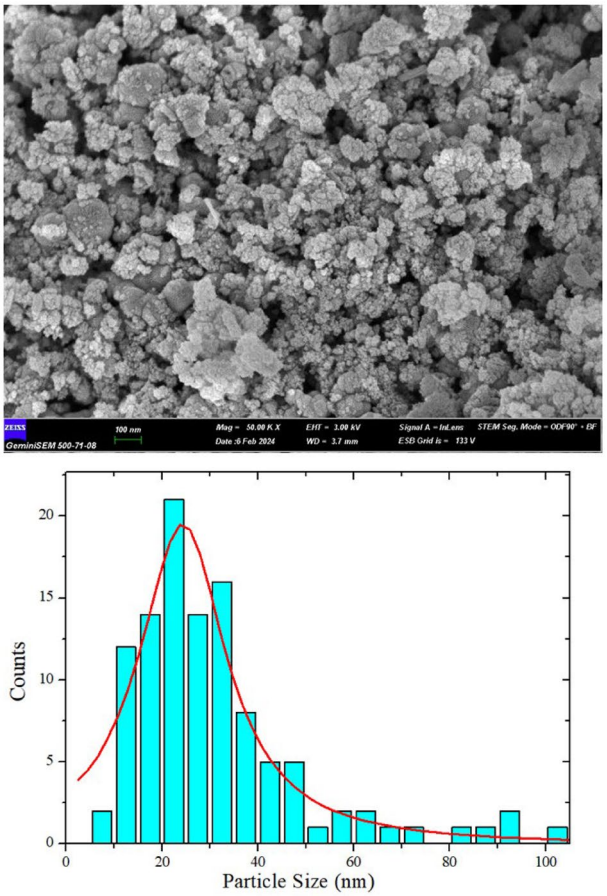

Fig. 4 FESEM image and particle size distribution histogram of $Fe_{74.5}Zr_{8.5}B_{17}$ MNPs

The FE-SEM images of amorphous $Fe_{74.5}Zr_{8.5}B_{17}$ MNPs are shown in Fig. 4. When Fig. 4 is examined, it is observed that the MNPs are mostly spherical

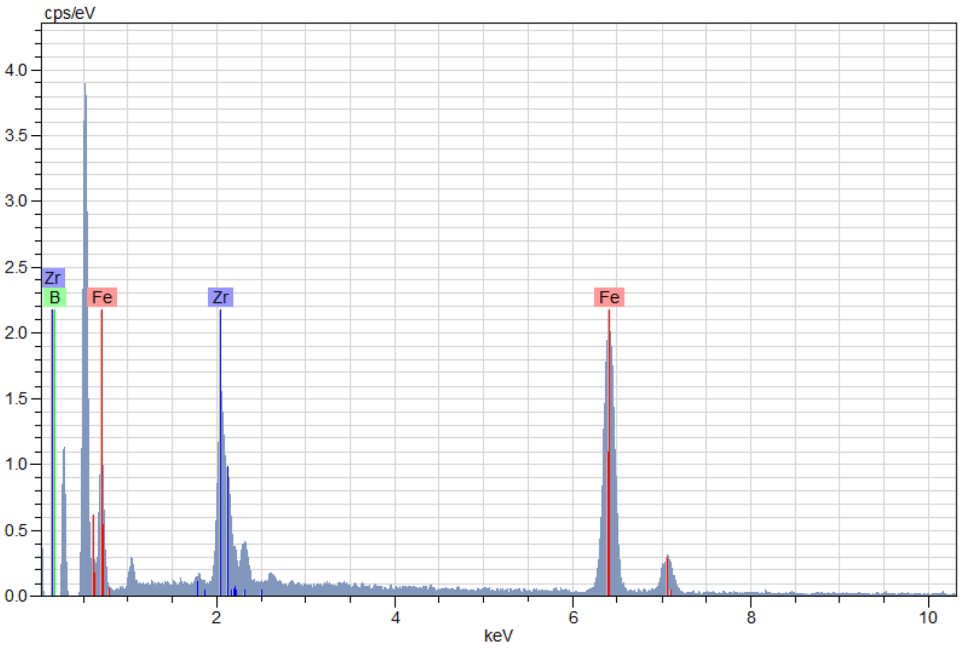

Fig. 5 The EDX pattern of amorphous $Fe_{74.5}Zr_{8.5}B_{17}$ MNPs

in structure and clustered due to the nature of their magnetic structure. Figure 4 also presents the particle size distribution histogram of MNPs. This analysis was performed by calculating the diameter of the distinct NPs observed in the FE-SEM image using the Image J (Image processing and analysis in java) program. As can be seen from the given graph, particle size distribution of MNPs was observed between 10 and 100 nm and it was determined that the most densely observed particle size of the MNPs was between 10 and 40 nm.

The EDX spectra of amorphous $Fe_{74.5}Zr_{8.5}B_{17}$ MNPs are shown in Fig. 5. EDX analysis of amorphous $Fe_{74.5}Zr_{8.5}B_{17}$ MNPs shows the presence of iron (Fe), zirconium (Zr), and boron (B) elements in the structure of MNPs. There were no other substantial peaks noted, suggesting that no impurities were present in the samples (the small peaks were due to the Au/Pd coating used). These findings indicated that amorphous $Fe_{74.5}Zr_{8.5}B_{17}$ MNPs were successfully synthesized.

The magnetic properties of amorphous $Fe_{74.5}Zr_{8.5}B_{17}$ MNPs obtained after the synthesis process were examined by VSM. The magnetic hysteresis loop is shown in Fig. 6. The hysteresis M-H loop at room temperature shows the typical geometric shape of a magnetic material loop. From the VSM curve observed in Fig. 6, the amorphous

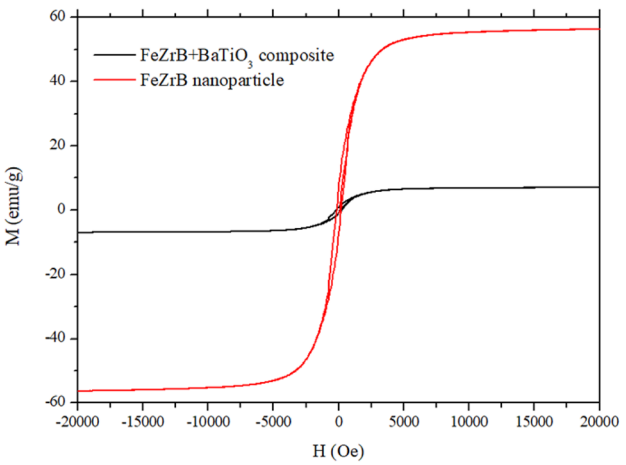

Fig. 6 Magnetization curves of amorphous $Fe_{74.5}Zr_{8.5}B_{17}$ MNPs and $Fe_7ZrB/BaTiO_3$ composite, which was heated at 400 °C for 30 min

$Fe_{74.5}Zr_{8.5}B_{17}$ MNPs have a saturation magnetization of 57.83 emu/g.

3.2 Crystallization kinetics

DTA curves obtained at different heating rates for amorphous $Fe_{74.5}Zr_{8.5}B_{17}$ MNPs are shown in Fig. 7. The crystallization onset (T_x) and peak temperatures (T_p) determined from the DTA curves are given in Table 1. It was observed that the peak temperature determined from the DTA curve for our sample as 467.18 °C is

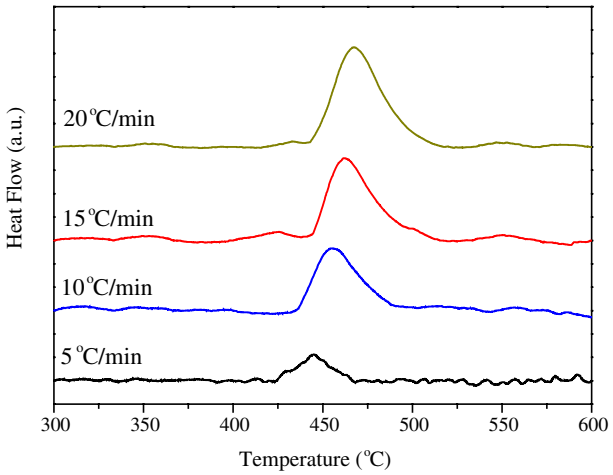

Fig. 7 DTA curves of amorphous $Fe_{74.5}Zr_{8.5}B_{17}$ MNPs measured at different heating rates

consistent with 471.8 °C obtained from the DSC curve for amorphous $Fe_{74.5}Zr_{8.5}B_{17}$ MNPs [17]. As the heating rate increases, both temperatures shift to higher values. The exothermic peaks observed in the DTA curves and their increase with heating rate are clear indicators of crystalline phase formation within the amorphous structure [18–20]. The thermal stability of amorphous alloys has a significant effect on their performance during applications. In this context, the activation energy provides information about the thermal stability of the alloy during the crystallization process. The Kissinger, Augis–Bennett, and Ozawa equations given below are widely used in the calculation of activation energy [21–23].

$$\ln\left(\frac{\beta}{T_p^2}\right) = -\frac{E_a}{R\,T_p} + const \tag{1}$$

$$\ln\left(\frac{\beta}{T_p - T_0}\right) = -\frac{E_a}{R\,T_p} + const \tag{2}$$

$$\ln(\beta) = -\frac{E_a}{R\,T_p} + const, \tag{3}$$

where β represents the heating rate, T_p stands for the temperature at the exothermal peak, R denotes the gas constant, T_0 signifies the absolute temperature, and E_a represents the activation energy. The activation energies for peak temperatures were determined from the slope of $\ln(\beta/T_p^2) - 1000/T_p$, $\ln(\beta/T_p - T_0) - 1000/T_p$, and $\ln(\beta) - 1000/T_p$ plots for three models. The Ozawa and Augis-Bennett plots are given in Fig. 8. Furthermore, the activation energies for peak onset temperatures were calculated from the slope of $\ln(\beta/T_x^2) - 1000/T_x$, $\ln(\beta/T_x - T_0) - 1000/T_x$ and $\ln(\beta) - 1000/T_x$. The E_a values for peak temperatures, using the Kissinger, Augis-Bennett, and Ozawa equations, were calculated as 276.02, 284.21, and 294.75 kJ/mol respectively. Correspondingly, the E_x values for crystallization onset temperatures were obtained as 228.20, 238.76, and 248.11 kJ/mol, respectively (Table 1). The increases in E_a and E_x values obtained from three different equations exhibit similar trends. The E_x value from the activation energy refers to nucleation, whereas the E_a value is associated with the growth process of the crystal structure. A smaller E_x value compared to E_a

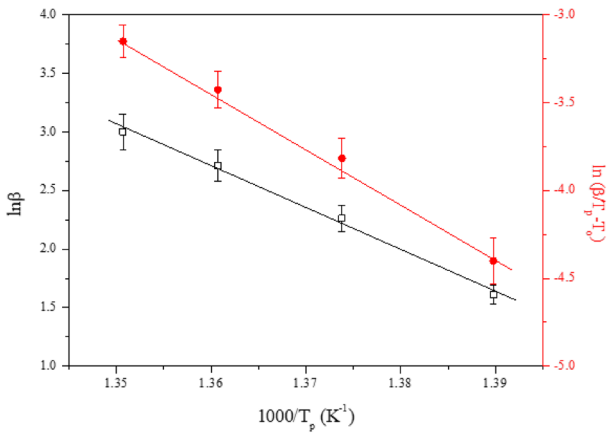

Fig. 8 Ozawa and Augis–Bennett plots of amorphous $Fe_{74.5}Zr_{8.5}B_{17}$ MNPs

Table 1 Kinetics parameters of amorphous $Fe_{74.5}Zr_{8.5}B_{17}$ MNPs

Heating rate (°C/min)	T_x (°C)	T_p (°C)	Kissinger	Augis–Bennett	Ozawa	*n*
5	423.04	446.36	E_x (kJ/mol)			1.87 ± 0.19
10	431.81	454.74	228.20 ± 2.3	238.76 ± 2.4	248.11 ± 2.5	
15	441.11	461.77	E_a (kJ/mol)			
20	446.08	467.18	276.02 ± 2.8	284.21 ± 8.53	294.75 ± 14.74	

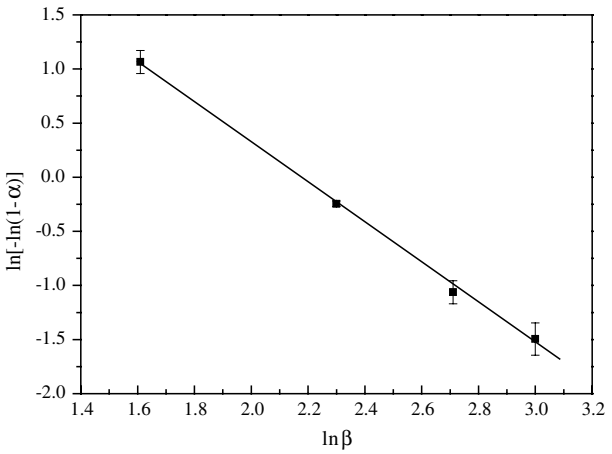

Fig. 9 According to the Ozawa method, the Avrami plots of amorphous $Fe_{74.5}Zr_{8.5}B_{17}$ MNPs

($E_x < E_a$) indicates a more challenging nucleation process during crystallization [20]. In this study, the activation energy calculated using the Kissinger method for amorphous $Fe_{74.5}Zr_{8.5}B_{17}$ MNPs was 276.02 kJ/mol. Previous studies have reported activation energy values for $CoFe_2O_4$, GeSbT MNPs, and Zr-based alloys as $E_a = 1.09$ eV/atom ~ 105 kJ/mol, $E_a = 2.22$ eV/atom ~ 214 kJ/mol, and E_a ~ 230 kJ/mol, respectively [15, 16, 24]. For FeBSi and Ni-based bulk amorphous alloys, the activation energy values were obtained as E_a ~ 326 kJ/mol and E_a ~ 435 kJ/mol, respectively [9, 16]. Based on these activation energy values, it can be inferred that the thermal stability of amorphous $Fe_{74.5}Zr_{8.5}B_{17}$ MNPs is higher than that of $CoFe_2O_4$, GeSbT NPs, and Zr-based alloys, but lower than that of FeSiB and Ni-based alloys [9, 14, 24–26]. The Avrami parameter "n" is utilized to explain the nucleation and growth mechanisms occurring during the crystallization process, and it is calculated from the exothermic peaks obtained from DTA measurements using the following equation [27].

$$\left.\frac{d\ln(-\ln(1-x))}{d\ln\beta}\right|_T = -n \tag{4}$$

At any given temperature, the value of x is determined by dividing the partial area (S) of the crystallization peak at that temperature by the total area (S_0) of the crystallization exotherm. Equation (4) suggests that for any constant temperature, the crystallization mechanism or Avrami exponent, denoted as n, can be derived from the slope of the resulting lines of the $\ln(-\ln(1-x)) - \ln(\beta)$ curve [27].

The temperature value of 460 °C was chosen for the calculation of the exothermic peaks' area. Figure 9 depicts the lnβ graph corresponding to ln(− ln(1 − x)) according to the Ozawa equation. The slope of the curve corresponds to the Avrami parameter. From this curve, the Avrami value for amorphous $Fe_{74.5}Zr_{8.5}B_{17}$ MNPs was determined as 1.87, indicating diffusion-controlled growth of small particles at decreasing nucleation rates during crystallization [28].

3.3 Magnetoelectric effect

The magnetoelectric effect (ME) represents a notable phenomenon where either a magnetic field (H) induces an electrical polarization or an electric field (E) induces magnetization. This intriguing phenomenon has captured the interest of the scientific community due to its promising applications in the development of next-generation magnetic field detectors, sensors, transducers, and biotechnology. Materials that display the magnetoelectric effect often possess a unique combination of magnetic and dielectric properties, making them highly sought after for advanced technological applications. These materials can be categorized into different classes, including single-phase multiferroics, composite multiferroics, and interface-induced multiferroics, each with its distinct mechanisms governing the magnetoelectric coupling [29–37].

In the phenomenon of direct magnetoelectric coupling, the ferromagnetic phase undergoes deformation through magnetostriction upon the application of a magnetic field. This deformation subsequently transfers strain to the ferroelectric phase at the interface, resulting in the generation of an electric signal [34–37]. Therefore, the transfer of strain between these two phases serves as the mechanism behind the ME coupling observed in composites. One of the main purposes of this study is to create two phases that do not react with each other to form impurities. Only the magnetic phase (FeZrB) applies mechanical constraints to $BaTiO_3$, generating a magnetoelectric voltage. This approach has been utilized in many magnetoelectric composite materials [34–37].

The electrical signal or the voltage induced in magnetoelectric materials has been measured by different methods. In our work, the magnetoelectric properties were evaluated utilizing a dynamic technique as

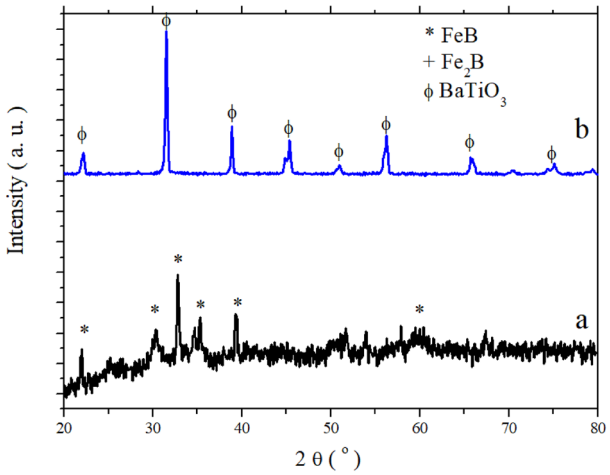

Fig. 10 XRD spectra of **a** FeZrB MNPs annealed at 550 °C for 30 min, **b** FeZrB-$BaTiO_3$ composite annealed at 400 °C for 30 min

detailed elsewhere [38–40]. A specialized configuration was employed, involving a modulated AC magnetic field alongside biased DC magnetic fields, to assess the changes in ME voltage (V_{AC}) of the sample. Both AC and DC magnetic fields were applied perpendicular to the sample surface. A lock-in amplifier (Model SR830, Stanford Research) was utilized to detect the ME output voltage. The ME coefficient (α) was determined using the formula, $\alpha = t \times \Delta H_{AC}/\Delta V_{AC}$. Here, ΔV_{AC} represents the amplitude of the induced ME voltage, t denotes the thickness of the sample, and ΔH_{AC} signifies the amplitude of the AC-modulated magnetic field.

$BaTiO_3$ NPs with dimensions of 30–35 nm were provided by the Nanografi company (Türkiye). Subsequently, the FeZrB MNPs we fabricated were combined with the $BaTiO_3$ NPs via ball milling at low speed, using a mass ratio of 30/70%. The resulting mixture underwent compression under 10 tons of pressure, forming pellets. These pellets, having a diameter of 13 mm and a thickness of 0.9 mm, were then subjected to heating at 400 °C for 30 min in an argon gas environment. As the crystallization temperature of the FeZrB sample is 467 °C, the heat treatment was conducted at a lower temperature. Furthermore, annealing of FeZrB at 550 °C for 30 min induces crystallization in the FeZrB MNPs, which is clearly evidenced by the X-ray spectra of samples subjected to elevated temperatures. (Fig. 10). Additionally, Fig. 10 clearly indicates that the FeZrB/$BaTiO_3$ composite, annealed at 400 °C, exhibits only $BaTiO_3$ peaks, with no traces of crystalline FeZrB phase peaks. Magnetization loop measurements showed that FeZrB/$BaTiO_3$ composite annealed at 400 °C has a saturation magnetization value of 7.5 emu/g, this sharp decrease in saturation values of composite is surely from the addition of non-magnetic $BaTiO_3$. 7.5 emu/g is slightly lower than the expected value, this could be due to the FeZrB phase loss during the annealing (Fig. 6). Since $BaTiO_3$ is a non-magnetic material, it only reduces the saturation magnetization. Apart from this, it does not cause any changes in parameters such as coercivity or remanent magnetization.

The SEM picture along with the elemental mapping (Fe, Zr, B, Ba, Ti, and O) analyzed via EDX on the polished surfaces of the FeZrB/$BaTiO_3$ composite is displayed in Fig. 11. Noticeable areas of light and dark contrast are evident in the SEM images. The lighter gray sections correspond to the grains of the $BaTiO_3$ phase, whereas the darker areas are recognized as the FeZrB phase. As seen from the color mapping, the predominantly blue and pink areas indicate the FeZrB phase, while the other areas represent the $BaTiO_3$ phase. It can be observed that the FeZrB phase disperses within the $BaTiO_3$ phase, ranging from very small sizes to clusters of approximately 1–2 μm.

Magnetoelectric voltage measured using lock-in amplifier as a function of applied AC magnetic field is given in Fig. 12 at zero DC magnetic field. The AC magnetic field at a frequency of 1 kHz varied between 0 and 150 Oe. FeZrB-$BaTiO_3$ composite shows a linear dependence of the magnetoelectric voltage on the AC magnetic field. The same measurements were performed at different AC magnetic field frequencies. The slope of this graph provides magnetoelectric coupling coefficient (α) values at frequencies of 1, 2, 5, 10, and 20 kHz for AC magnetic fields, which are 8.9, 19.6, 62.6, 142, and 303 mV/Oe/cm, respectively. It was noted that the magnetoelectric coupling coefficient rises with increasing H_{AC} frequency. Additionally, no resonant behavior was observed within the investigated frequency range. Various types of connective structures have been explored to improve magnetoelectric coupling. These include particulate composites [41], films, core–shell NPs, [42], nanofibers [43], etc. Recently, attention has shifted toward magnetoelectric nanocomposites [44], driven by the growing need for high-performance, multifunctional, compact, and cost-effective electronic components [45]. In some previous studies, the magnetoelectric coupling coefficient (α)

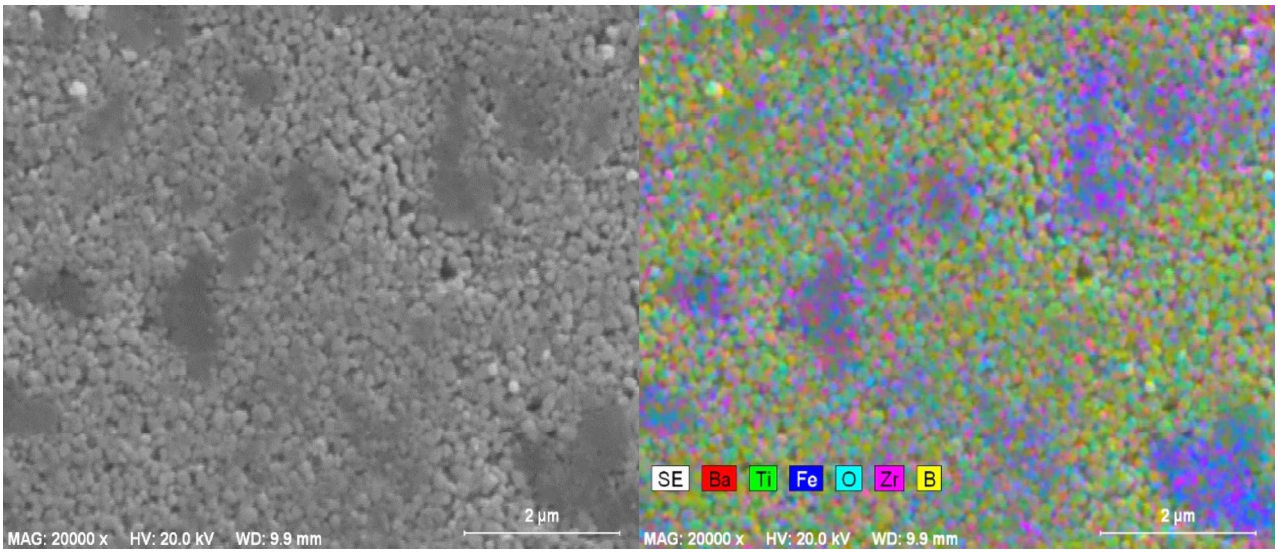

Fig. 11 SEM image and color mapping of FeZrB-$BaTiO_3$ composite

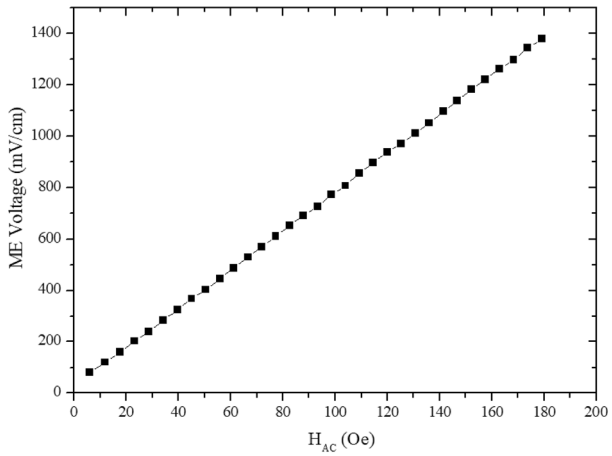

Fig. 12 Variation of magnetoelectric voltage as a function of applied AC magnetic field

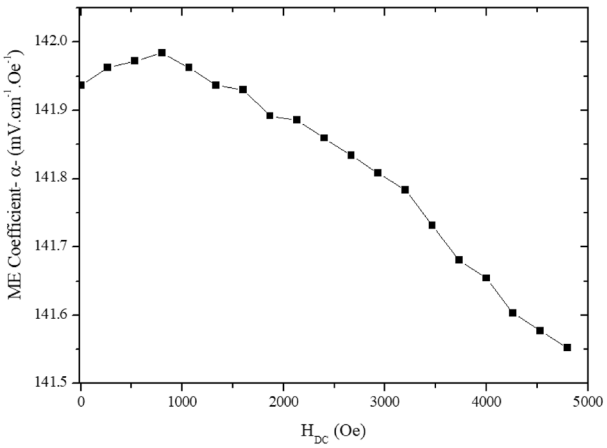

Fig. 13 Effect of DC magnetic field on magnetoelectric coefficient

values have been reported as follows: 10 mV/cm·Oe for $NiFe_2O_4/BaTiO_3$ composites [46], 1.48 mV/cm·Oe for $CoFe_2NiFeO_4/BaTiO_3$ composites [47, 48], 50.2 mV/cm·Oe for $MgFe_2NiFeO_4/BaTiO_3$ composites [50], and 7 mV/cm·Oe for $BiFeO_3$ composites [48]. The α value obtained in this study is comparable in magnitude to those reported in some of the previous studies.

In Fig. 13, the dependence of the magnetoelectric coupling coefficient on the DC magnetic field is illustrated at 12.5 Oe applied H_{AC} magnetic field with a frequency of 10 kHz. FeZrB NPs, known for their positive magnetostrictive properties, induce a strain parallel to the H_{DC} magnetic field, leading to polarization of the $BaTiO_3$ NPs. Initially, the magnetoelectric coupling coefficient rises with the applied DC magnetic field, reaching a peak value before declining. This pattern mirrors findings from previous studies by different research groups [36]. The initial increase in the magnetoelectric coupling coefficient is attributed to the growing magnetostriction of FeZrB under the influence of the applied DC field. Magnetostriction reaches its maximum at a specific magnetic field, beyond which it causes only marginal changes in polarization. Consequently, the

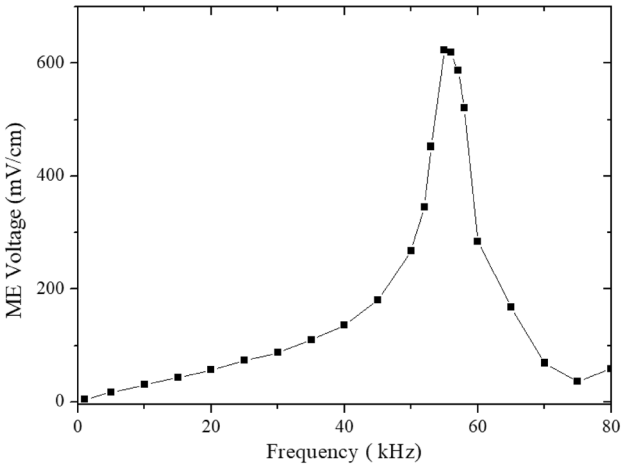

Fig. 14 Variation of magnetoelectric voltage as a function of frequency of AC magnetic field

magnetoelectric coupling coefficient diminishes with further increments in the magnetic field.

It has been realized that resonance enhancement of the ME response may be expected when the modulation frequency of the applied fields coincides with the magnetic, electrical, or mechanical modes of the system under study. The frequency dependence of ME voltage is shown in Fig. 14. For our sample, the optimum frequency is about 55 kHz, which is approximately the same as in some studies [49] and slightly lower than in others [50].

4 Conclusion

In conclusion, this study reports for the first-time crystallization kinetics of FeZrB MNPs and magnetoelectric properties of FeZrB/$BaTiO_3$ composite. For this purpose, the amorphous $Fe_{74.5}Zr_{8.5}B_{17}$ MNPs were successfully obtained by a simple chemical reduction method using $NaBH_4$ as reduction agent. Subsequently, the FeZrB MNPs were combined with the $BaTiO_3$ NPs via ball milling at low speed, using a mass ratio of 30/70%, respectively. Based on the observations and the analyses, the results are summarized as follows:

(i) Characterization findings performed with EDX clearly revealed the elemental composition. The findings obtained from XRD showed that the MNPs have amorphous structure.

(ii) The magnetization values are about 57.83 and 7.5 emu/g for amorphous $Fe_{74.5}Zr_{8.5}B_{17}$ MNPs and FeZrB/$BaTiO_3$ composite, respectively. The decrease in the saturation value of the composites was due to the presence of non-magnetic $BaTiO_3$.

(iii) Crystallization peak temperature (T_p) and E_a were determined as 467.18 °C and 294 kJ/mol, respectively.

(iv) In addition, the magnetoelectric coefficient value measured in a 1 kHz AC magnetic field was determined as approximately 8.9 mV/Oe/cm. Taken together, our study indicated that the FeZrB/$BaTiO_3$ composite can be a potential candidate material for developing novel magnetoelectric materials.

Acknowledgements

This study was supported by Scientific and Technological Research Council of Türkiye (TUBITAK) under the Grant Number 123M414. The authors thank to TUBITAK for their supports. We would also like to thank Inonu University BAP unit for supporting this study with the project code number FDP-2024-3385. The authors acknowledge that Biorender.com was used for making Figs. 1 and 2.

Author contributions

GD contributed toward writing—original draft, methodology, investigation, and data curation. EBK contributed toward methodology and investigation. AU contributed toward writing—original draft, methodology, investigation, and data curation. NB contributed toward methodology and investigation. BA contributed toward writing—original draft, methodology, investigation, and data curation. SA contributed toward Writing—review & editing, formal analysis, investigation, and funding acquisition. All authors reviewed the manuscript.

Funding

Open access funding provided by the Scientific and Technological Research Council of Türkiye

(TÜBİTAK). The funding was provided by Scientific and Technological Research Council of Türkiye (TUBITAK) under the Grant Number 123M414.

Data availability

Data will be made available on request.

Declarations

Conflict of interest The authors declare that they have no known competing financial interests or personal relationships that could have appeared to influence the work reported in this paper.

Ethical approval Ethical approval is not applicable for this article.

Open Access This article is licensed under a Creative Commons Attribution 4.0 International License, which permits use, sharing, adaptation, distribution and reproduction in any medium or format, as long as you give appropriate credit to the original author(s) and the source, provide a link to the Creative Commons licence, and indicate if changes were made. The images or other third party material in this article are included in the article's Creative Commons licence, unless indicated otherwise in a credit line to the material. If material is not included in the article's Creative Commons licence and your intended use is not permitted by statutory regulation or exceeds the permitted use, you will need to obtain permission directly from the copyright holder. To view a copy of this licence, visit http://creativecommons.org/licenses/by/4.0/.

References

1. D. Nykypanchuk, M.M. Maye, D. van der Lelie, O. Gang, Nature **451**, 549–552 (2008)
2. C. Yee, G. Kataby, A. Ulman, T. Prozorov, H. White, A. King, M. Rafailovich, J. Sokolov, A. Gedanken, Langmuir **15**, 7111–7115 (1999)
3. K.V.P.M. Shafi, A. Ulman, X.Z. Yan, N.L. Yang, C. Estournes, H. White, M. Rafailovich, Langmuir **17**, 5093–5097 (2001)
4. M. Tadic, S. Kralj, M. Jagodic, D. Hanzel, D. Makovec, Appl. Surf. Sci. **322**, 255–264 (2014)
5. Z.H. Guo, K. Shin, A.B. Karki, D.P. Young, R.B. Kaner, H.H. Thomas, J. Nanopart. Res. **11**, 1441–1452 (2009)
6. G. Dik, A. Ulu, B. Ates. Medicinal and Biological Application of Magnetic Alloy Nanoparticles and Their Polymer Nanocomposites. In: Thomas, S., Rezazadeh Nochehdehi, A. (eds) Handbook of Magnetic Hybrid Nanoalloys and their Nanocomposites. Springer, Cham. https://doi.org/10.1007/978-3-030-90948-2_32
7. A.H. Lu, E.E. Salabas, F. Schüth, Angew. Chem. Int. Ed. **46**, 1222–1244 (2007)
8. M. Colombo, S. Carregal-Romero, M.F. Casula, L. Gutiérrez, M.P. Morales, I.B. Böhm, J.T. Heverhagen, D. Prosperi, W.J. Parak, Chem. Soc. Rev. **41**, 4306–4334 (2012)
9. G.D. Forster, L.F. Barquín, R.L. Bilsborrow, Q.A. Pankhurst, I.P. Parkin, W.A. Steer, J. Mater. Chem. **9**, 2537–2544 (1999)
10. H. Kobori, K. Uzimoto, A. Hoshino, A. Yamasaki, A. Sugimura, T. Taniguchi, T. Horie, Y. Naitoh, T. Shimizu, J. Supercond. Nov. Magn. **25**, 2809–2812 (2012)
11. S. Singh, N. Kumar, A. Jha, M. Sahni, K.D. Sung, J.H. Jung, S. Chaubey, J. Mater. Sci. Mater. Electron. **26**, 32–36 (2015)
12. H. Li, Y. Yang, C. Chen, D. Chen, Y. Zhang, Y. Meng, Z. Zhang, J. Mater. Sci. Mater. Electron. **35**, 1076 (2024)
13. Y. Slimani, H. Erdemi, A. Baykal, M.A. Almessiere, A. Thakur, K.M. Batoo, J. Phys. Chem. **195**, 112292 (2024)
14. B. Ramakrishna Rao, A.K. Shah, M. Srinivas, J. Bhatt, A.S. Gandhi, B.S. Murty, Metall. Mater. Trans. A **42**, 3913–3920 (2011)
15. D.B. Do, N.D. Phu, N.V. Hung, L.H. Hoang, L.T.M. Oanh, D.M. Thanh, N.V. Minh, IEEE Trans. Magn. **50**, 2502904 (2014)
16. B. Chen, G.H. Ten Brink, G. Palasantzas, B.J. Kooi, J. Phys. Chem. C **121**, 8569–8578 (2017)
17. J. Wang, M. Fan, X. Bian, M. Yu, T. Wang, S. Liu, Y. Yang, Y. Tian, R. Guan, J. Magn. Magn. Mater. **465**, 480–488 (2018)
18. N. Bayri, T. Izgi, H. Gencer, P. Sovak, M. Gunes, S. Atalay, J. Non-Cryst, Solids **355**, 12–16 (2009)
19. H. Gencer, T. Izgi, V.S. Kolat, N. Bayri, A.O. Kaya, S. Atalay, J. Non-Cryst, Solids **379**, 185–191 (2013)
20. X. Wu, X. Li, S. Li, Mater. Res. Express **7**, 016118 (2020)
21. H.E. Kissinger, J. Res. Natl. Bur. Stand. **57**, 217–221 (1956)
22. J.A. Augis, J.E. Bennett, J. Therm. Anal. **13**, 283–292 (1978)
23. T. Ozawa, Bull. Chem. Soc. Jpn **35**, 1881–1886 (1965)

24. L. Liu, Z.F. Wu, J. Zhang, J. Alloys Compd. **339**, 90–95 (2002)
25. D.S. Santos, D.R. Santos, J. Non-Cryst, Solids **304**, 56–63 (2002)
26. F.X. Qin, H.F. Zhang, B.Z. Ding, Z.Q. Hu, Intermetallics **12**, 1197–1203 (2004)
27. T. Ozawa, J. Therm. Anal. **3**, 301–324 (1970)
28. L. Guo, Q. Zhu, Z. Chen, K. Zhang, Y. Jiang, J. Non-Cryst, Solids **577**, 121310 (2022)
29. H. Zheng, J. Wang, S.E. Lofland, Z. Ma, L. Mohaddes-Ardabili, T. Zhao, L. Salamanca-Riba, S.R. Shinde, S.B. Ogale, F. Bai, D. Viehland, Y. Jia, D.G. Schlom, M. Wutting, A. Roytburd, R. Ramesh, Science **303**, 661–663 (2004)
30. C.V. Nan, M.I. Bichurin, S.X. Dong, D. Viehland, G. Srinivasan, J. Appl. Phys. **103**, 031101 (2008)
31. M. Fiebig, J. Phys. D Appl. Phys. **38**, R123–R152 (2005)
32. W. Eerenstein, N.D. Mathur, J.F. Scott, Nature **442**, 759–765 (2006)
33. N.A. Spaldin, R. Ramesh, Nat. Mater. **18**, 203–212 (2019)
34. J.Q. Gao, Z.K. Jiang, S.J. Zhang, Z.N. Mao, Y. Shen, Z.Q. Chu, Actuators **10**, 109 (2021)
35. A. Plyushch, D. Lewin, A. Sokal, R. Grigalaitis, V.V. Shvartsman, J. Macutkevic, S. Salamon, H. Wende, K.N. Lapko, P.P. Kuzbir, D.C. Lupascu, J. Banys, J. Alloys Compd. **917**, 165519 (2022)
36. A.S. Kumar, C.S.C. Lekha, S. Vivek, V. Saravanan, K. Nandakumar, S.S. Nair, J. Magn. Magn. Mater. **418**, 294–299 (2016)
37. T.R. Nizamov, A.A. Amirov, T.O. Kuznetsova, I.V. Dorofievich, I.G. Bordyuzhin, D.G. Zhukov, A.V. Ivanova, A.N. Gabashvili, N.Y. Tabachkova, A.A. Tepanov, I.V. Shchetinin, M.A. Abakumov, A.G. Savchenko, A.G. Majouga, Nanomaterials **13**, 811 (2023)
38. M.M. Vopson, Y.K. Fetisov, G. Caruntu, G. Srinivasan, Materials **10**, 963 (2017)
39. J.M. Caicedo, J.A. Zapata, M.E. Gomez, P. Prieto, J. Appl. Phys. **103**, 07E306 (2008)
40. K. Gil, J. Gil, B. Cruz, A. Ramirez, M. Medina, J. Torres, J. Phys. Conf. Ser. **687**, 012090 (2016)
41. H. Ryu, P. Murugavel, J.H. Lee, S.C. Chae, T.W. Noh, Y.S. Oh, H.J. Kim, K.H. Kim, J.H. Jang, M. Kim, C. Bae, J.G. Park, Appl. Phys. Lett. **89**, 102907 (2006)
42. M. Reaz, A. Haque, K. Ghosh, Nanomater. **10**, 563 (2020)
43. Q. Zhang, J. Zhu, H. Liu, X. Fei, M. Zhu, Adv. Funct. Mater. **34**, 2309968 (2024)
44. F. Narita, M. Fox, Adv. Eng. Mater. **20**, 1700743 (2018)
45. J.P. Zhou, L. Lv, Q. Liu, Y.X. Zhang, P. Liu, Sci. Technol. Adv. Mater. **13**, 045001 (2012)
46. V. Corral-Flores, D. Bueno-Baques, R.D. Ziolo, Acta Mater. **58**, 764–769 (2010)
47. V. Corral-Flores, D. Bueno-Baques, D. Carrillo-Flores, J.A. Matutes-Aquino, J. Appl. Phys. **99**, 08J503 (2006)
48. S.Y. Tan, S.R. Shannigrahi, S.H. Tan, F.E.H. Tay, J. Appl. Phys. **103**, 094105 (2008)
49. J.M. Caicedo, J.A. Zapata, M.E. Gómez, P. Prieto, J. Appl. Phys. **103**, 07E306 (2008)
50. N. Murali, D. Mukherjee, S.B. Das, A.K. Dhillon, S. Siddhanta, D. Mallick, S. Betal, Adv. Eng. Mater. **25**, 2301061 (2023)

Publisher's Note Springer Nature remains neutral with regard to jurisdictional claims in published maps and institutional affiliations.